General and Reliable Azimuthal Alignment Algorithm for Low Loss Multicore Fiber Fusion Splicing

Tristan Kremp , *Senior Member, Optica*, Yue Liang , *Member, IEEE*, and Alan H. McCurdy, *Member, IEEE*

Abstract—Multicore fiber is a promising spatial division multiplexing technology to increase the transmission bandwidth of optical fiber links in any given available spatial cross section. To connect multicore fibers, similar to single-core fibers, fusion splicing is an indispensable tool. Since multicore fibers cannot be circularly symmetric, precise transverse and azimuthal alignment is crucial to minimize the insertion loss penalty that would originate from even small offsets in the core locations of the two fibers to be spliced together. In this paper, a novel azimuthal alignment algorithm for multicore fiber splicing is presented. Since it is based on side-view images, it can also determine the twist rates of both fibers to be spliced and take these twist rates into account when calculating the optimum azimuthal alignment angle at the very ends of the two fibers. In the case of fibers with markers, i.e., fibers that are not rotationally symmetric, the relative and absolute polarities of the two fiber ends are computed as well. We present the formulation of the azimuthal alignment algorithm and demonstrate its stability and versatility for a wide range of fibers with vastly different geometries, core numbers and twist rates, including an offset single-core fiber. In the case of 4-core fibers with markers, we achieve average splice losses of less than 0.03 dB regardless of the polarity, which is a substantial advantage in terms of real-world applicability in the field. For a twisted 7-core fiber, we demonstrate an accurate twist rate detection with standard deviation < 1.4/m (turns per meter).

Index Terms—Fusion splicing, multicore fiber, spatial division multiplexing.

I. INTRODUCTION

WHILE bandwidth demands continue to grow exponentially, multicore fiber (MCF) allows to increase the density of optical channels in the available space, e.g., in the ducts of hyperscale data centers or inside the armored protection layer of submarine communication cables. For the deployment of optical fiber and cable, fusion splicing of opposing fiber ends is a crucial step to maintain low insertion loss. Using the cross-correlation of side-view images for 4-core or 8-core fibers, fusion splice losses of about 0.5 dB were reported in [1],

which these authors found to be comparable to the results from splicing with an optical source and a power meter (LID – Local Injection and Detection System) that monitors the insertion loss during the alignment optimization. Lower splice losses of 0.08–0.18 dB for the center core and 0.1–1.0 dB for the six outer cores of a symmetric 7-core fiber were reported in [2] using a so-called interrelation profile analysis (IPA) method [3]. With an improved IPA2 version of this method, an average splice loss of 0.092 dB for a 4-core fiber with marker [4] and 0.2 dB with 80% success rate for a low-crosstalk trench-assisted 4-core fiber with marker [5] were reported. With a field-usable compact fusion splicer, 0.12 dB splice loss was achieved [6] for a 5-core fiber. Reverse-tapering the smaller of two spacing-mismatched 7-core fibers, 0.17 dB insertion loss was reported in [7]. Applying a similar thermal technique that expands the cross section at the ends of two identical coupled-core 4-core fibers, a minimum splice loss of 0.02 dB was achieved [8], but at the expense of increasing the power coupling between cores by 20 dB, which may be beneficial for such coupled-core MCF, but is detrimental for uncoupled-core MCF applications where channel crosstalk should be minimized. Using Fourier-based methods for fibers with 180°-periodicity, e.g., polarization maintaining fibers with stress rods, mean extinction ratios higher than 30 dB [9] and in the range of (32±2.74) dB [10], as well as azimuthal angle errors of (1.06±0.92) degrees [11] were achieved. While all these methods were side-view based, an end-view based method [12] was reported to give an average fusion splice loss of 0.09 dB for the inner core and 0.18 dB for the outer cores of a dual-ring 12-core fiber.

We recently developed a novel azimuthal alignment algorithm and achieved an average splice loss in 4-core MCF of less than 0.03 dB [13] with a 3-electrode arc-discharging fusion splicer [14]. This is near the level of typical single-core fiber splice losses, which are usually below 0.03 dB for active core alignment and around 0.04 dB for active cladding alignment, where "active" refers to individual geometrical adjustments of the transverse alignment using side-view images (PAS – Profile Alignment System).

However, MCF fusion splicing not only needs to provide low insertion loss, i.e., alignment accuracy, but also has to guarantee that the correct cores, i.e., transmission signal channels, are being aligned. This can be achieved by comparing, at both fiber ends, the symmetry-breaking location of a "marker", which is usually a small core-like refractive index change [15] or an
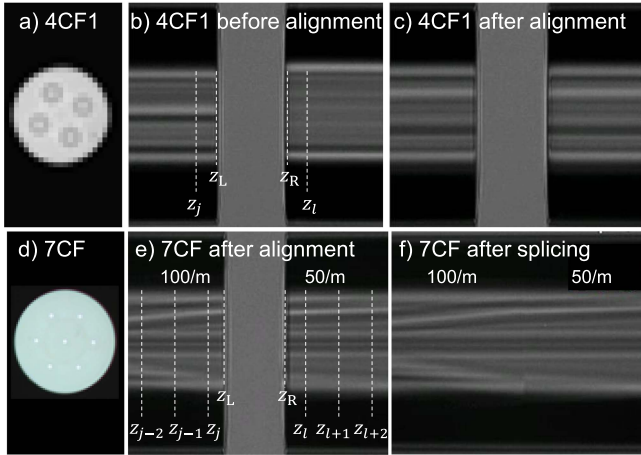
Fig. 1. End-view and side-view images, illustrating the end locations z_L and z_R of the left and right fiber, respectively, as well as the locations z_j and z_l for the azimuthal scans and the twist rates of the twisted fibers [13], [18]. (a) End-view of 4CF1. (b,c) Side-view of two ends of untwisted 4CF1 before and after azimuthal alignment. (d) End-view of 7CF. (e,f) Side-view of two ends of 7CF with twist rates of approximately 100/m and 50/m, respectively, after alignment and fusion splicing, showing a perfect match, including the inavoidable kink of the cores at the location of the splice due to the different twist rates.
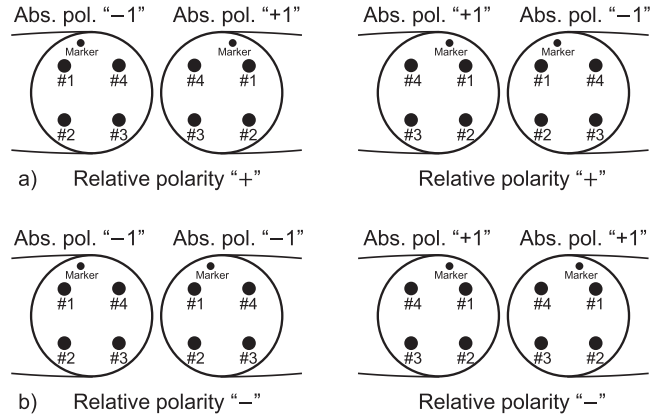

Fig. 2. Absolute and relative polarity conventions and core numbers in the example of 4CF. If a clockwise rotation of the marker brings the marker closer to the closest core, then the absolute polarity of this fiber end is "+1", otherwise "−1". (a) Relative polarity "+": The two opposing fiber ends have different absolute polarities. (b) Relative polarity "−": The two opposing fiber ends have identical absolute polarities. In this case, the markers and cores cannot be all aligned simultaneously.
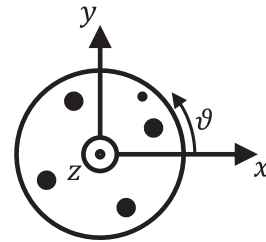

Fig. 3. Coordinate system in end-view for a 4-core fiber with marker.

asymmetry such as a D-shape [16] of the surrounding cladding. Such an asymmetric feature thus also allows to uniquely distinguish individual cores as well as the two ends of the fiber, i.e., it can be used to assign a "polarity" to each end. While it is preferable to flip the two fibers such that they have the correct relative polarities in the splicer, it would be much easier if the alignment algorithm is able to achieve the same low splice loss and correct channel alignment for any combination of polarities.

Furthermore, in applications such as 3D shape sensing [17], the fiber cores may be subject to significant twist that changes the optimal alignment angle along the fiber and therefore needs to be quantitatively taken into account in side-view-based imaging to achieve the lowest possible splice loss.

In this work, we therefore formulate the novel azimuthal alignment algorithm from [13] in detail and generalize it such that it can also determine the twist rates as well as the relative and absolute polarities of the two fiber ends in a side-view-based fusion splicer. We demonstrate accurate alignment for a wide range of fibers with vastly different geometries, core numbers and twist rates. In particular, for two different 4-core fiber designs, we achieved a very low and polarity-independent average splice loss of less than 0.03 dB as well as a >95% reliable polarity detection among more than 200 trials. For a twisted 7-core fiber, we demonstrate an accurate twist rate detection with standard deviation < 1.4/m.

II. SIDE-VIEW IMAGES AND SINOGRAMS

In the present study, we use the Fitel S185PM ROF fusion splicer hardware [14] and two very similar MCF designs with 4 cores and a marker ("4CF1" and "4CF2"), as well as twisted 7-core fiber ("7CF") without a marker, 8-core fiber with a marker ("8CF"), 2-core fiber without marker ("2CF") and offset single-core fiber ("1CF"). Fig. 1 shows end-view and side-view images

before and after alignment and fusion splicing of 4CF1 and 7CF with different twist rates in units of turns per meter (1/m).

If a fiber has a marker, e.g., the 4-core fiber 4CF1 in Fig. 1(a), then its marker is necessarily located at an asymmetric position (see Fig. 2), and thus not only allows to uniquely identify individual cores, but also allows to uniquely identify each end of a single MCF. This binary identifier is often referred to as the absolute polarity of the fiber, which we here refer to with the values "+1" and "−1", similar to the "north" and "south" poles of a magnet. We define the core numbers such that they increase clockwise on the "+1" end and counterclockwise on the other end ("−1") of the fiber. When splicing two ends of different fibers, their absolute polarities can either be different ("correct" relative polarity "+") or identical ("wrong" relative polarity "−"), see Fig. 2. Hence, in our notation, the relative polarity is the product of the number −1 and the two absolute polarities. We note that when a fiber is cut, the two ends at the cut have different absolute polarities ("+1", "−1") and "correct" relative polarity "+", in agreement with the trivial fact that before making the cut, the marker inside the fiber was perfectly aligned with itself.

In the following mathematical analysis, the angle ϑ denotes the azimuthal orientation of the fiber relative to the splicer camera plane in Fig. 1(b), (c), (e), and (f), z is the longitudinal location along the fiber, and x is the transverse coordinate parallel to the camera plane (x, z). The corresponding coordinate system is shown in Fig. 3. Thus, Fig. 1(b), (c), (e), and (f)
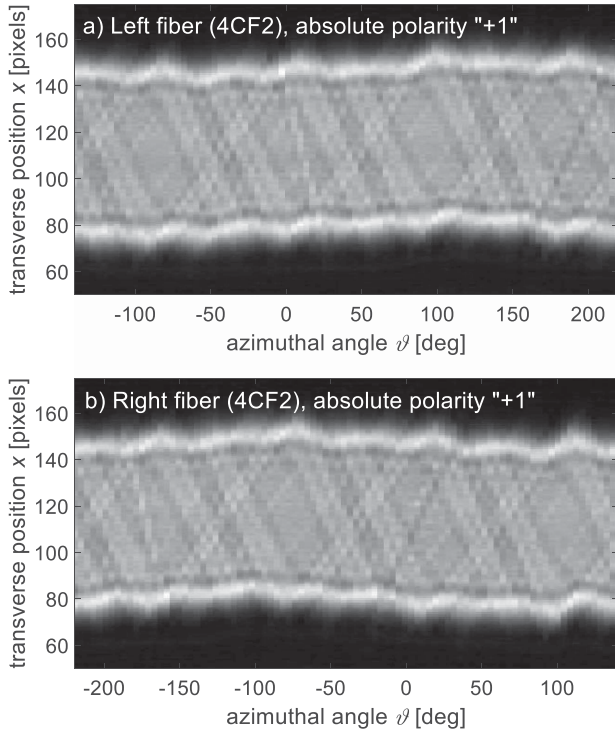
Fig. 4. Side-view sinograms of two opposing ends of fiber 4CF2 with identical absolute polarities, i.e., wrong relative polarity "−". (a) $I(\vartheta, y, z_{\mathrm{L},1})$ of left fiber (4CF2) with absolute polarity "+1". (b) $I(\vartheta, y, z_{\mathrm{R},1})$ right fiber (4CF2) with absolute polarity "+1".

show the side-view projection intensity $I(\vartheta, x, z)$ for one fixed azimuthal orientation ϑ of the two fibers to be spliced. Choosing instead a fixed location, e.g., $z = z_j$ close to the end z_{L} of the left fiber, we refer to the resulting function $I(\vartheta, x, z_j)$ as a side-view sinogram, which is a series of cross-sectional intensity scans at different azimuthal orientations ϑ but at the same location z_j. If a side-view sinogram is not perfectly straight, e.g., because a fiber happens not to be exactly parallel to the axis of the rotational motor as in the case of fiber 4CF2 in Fig. 4, the accuracy of the algorithm that we describe in the following Section III can be further improved by numerically straightening the side-view sinogram as a pre-processing step [19].

III. DISCRETIZATION AND CROSS-CORRELATION ALGORITHM

Correlating side-view sinograms that are taken at longitudinal locations z_j and z_l near the ends z_{L} and z_{R} of the left and right fiber to be spliced, we define the (global) cross-correlation

$$c^{(j,l)}(\vartheta, x) = \int I(\vartheta', x, z_j) \, I(\vartheta' + \vartheta, x, z_l) \, \mathrm{d}\vartheta'. \quad (1)$$

For the following azimuthal alignment computations, the originally continuous variables ϑ, x, z will need to take on discrete values associated, e.g., with the angular resolution of the rotational motor and pixel locations on the camera. We therefore choose N azimuthal angles ϑ_n around the fiber axis, K transverse positions x_k, and L longitudinal locations z_l (or z_j) along the length of the fiber. These three sets of numbers do not need to be equispaced, i.e., differences between neighboring

points are allowed to vary. The total numbers N, K, L are nonnegative integers, using the counting indices $n = 1, \ldots, N$, $k = 1, \ldots, K$, $l = 1, \ldots, L$.

To also discretize the side-view projection intensity $I(\vartheta, x, z)$, L so-called "sinogram" matrices $\boldsymbol{S}^{(l)}$ of dimension $N \times K$ are defined, where each of these matrices represents the intensity at $z = z_l$ for the discretized transverse positions $x_1 \ldots x_K$ while the associated fiber is being rotated through all of the defined N discrete rotation angles. Thus, the entries of the matrix $\boldsymbol{S}^{(l)}$ are

$$S_{n,k}^{(l)} = I(\vartheta_n, x_k, z_l), \quad n = 1, \ldots, N, \ k = 1, \ldots, K. \quad (2)$$

In Fig. 1(b), as in most cases when splicing untwisted fiber, we have $L = 2$ longitudinal locations, namely, $z_j = z_1$ and $z_l = z_2$, and the alignment analysis is thus in this case based upon a pair of sinogram matrices $\boldsymbol{S}^{(1)}$ and $\boldsymbol{S}^{(2)}$.

To avoid mathematical ambiguities, the azimuthal angles ϑ_n are assumed to be distinct even after applying the modulo-2π-command, i.e., $\mathrm{mod}(\vartheta_n, 2\pi) \neq \mathrm{mod}(\vartheta_m, 2\pi)$ whenever $n \neq m$. In complex-valued notation with the imaginary unit i, this is equivalent to $\mathrm{e}^{\mathrm{i}\vartheta_n} \neq \mathrm{e}^{\mathrm{i}\vartheta_m}$ whenever $n \neq m$. As a result, a regular matrix $\boldsymbol{F}$ may be defined (azimuthal inverse discrete Fourier transform, nonuniform if the angles ϑ_n are not equispaced, see also Appendix: Equidistant Angles for FFT) of dimension $N \times N$ that has complex-valued entries

$$F_{n,m} = \frac{1}{N} \mathrm{e}^{\mathrm{i}(m-1)\vartheta_n}, \quad n, m = 1, \ldots, N. \quad (3)$$

Using the indexing convention from (3), the first column $m = 1$ of the matrix $\boldsymbol{F}$ describes a zero angular frequency, i.e., the angle-invariant constant ("DC") part. Since the matrix $\boldsymbol{F}$ is regular, the linear system

$$\boldsymbol{F}\tilde{\boldsymbol{S}}^{(l)} = \boldsymbol{S}^{(l)} \quad (4)$$

has a unique solution matrix $\tilde{\boldsymbol{S}}^{(l)}$ of dimension $N \times K$. For notational clarity, the tilde accent "~" is used for Fourier domain quantities. The k-th column of the matrix $\tilde{\boldsymbol{S}}^{(l)}$ contains the set of N discrete Fourier coefficients of the discrete sinogram $\boldsymbol{S}^{(l)}$ at the transverse position x_k and longitudinal location z_l. It is noted that if $\boldsymbol{F}$ was not regular, for instance because the above distinctness assumption ($\mathrm{e}^{\mathrm{i}\vartheta_n} \neq \mathrm{e}^{\mathrm{i}\vartheta_m}$ whenever $n \neq m$) was not true, then (4) can still be approximately solved in a least-squares sense by using the pseudoinverse of the matrix $\boldsymbol{F}$.

To further simplify the following notation, the asterisk "∗" is used to denote complex conjugate (without transposing) and the symbol "⊙" (\odot) for the element-wise (Hadamard) multiplication of two matrices of equal dimension. The element-wise product of the matrix $\tilde{\boldsymbol{S}}^{(l)}$ (e.g., Fourier transform of Fig. 4(a)) and a complex-valued or real-valued matrix $\tilde{\boldsymbol{S}}^{(j)}$ (e.g., Fourier transform of Fig. 4(b)) of equal dimension $N \times K$ may be built using the following relation:

$$\tilde{\boldsymbol{C}}^{(j,l)} = \tilde{\boldsymbol{S}}^{(j)*} \odot \tilde{\boldsymbol{S}}^{(l)}. \quad (5)$$

Thus, the complex-valued or real-valued matrix $\tilde{\boldsymbol{C}}^{(j,l)}$ also has the dimension $N \times K$ and contains the discrete Fourier

coefficients of the cross-correlation of $\boldsymbol{S}^{(j)}$ and $\boldsymbol{S}^{(l)}$, which will be the basis of the separation analysis in Section IV.

In order to maintain the physical integrity of the fiber endfaces, all transverse positions need to be subject to the same angular correction. Hence, the information from all transverse positions x_k needs to be combined. Therefore, a suitable set of real-valued or complex-valued transverse weights $\{w_k\}_{k=1}^{K}$ is used (at least one of the w_k needs to be nonzero) to build a weighted sum of all columns of the matrix $\tilde{\boldsymbol{C}}^{(j,l)}$ from (5), i.e., a column vector $\tilde{\boldsymbol{c}}^{(j,l)}$ with complex-valued entries [19]

$$\tilde{c}_n^{(j,l)} = \sum_{k=1}^{K} w_k \tilde{C}_{n,k}^{(j,l)}, \quad n = 1, \ldots, N. \tag{6}$$

Finally, the Fourier transform from (4) is undone by applying the transformation matrix $\boldsymbol{F}$:

$$\boldsymbol{c}^{(j,l)} = \boldsymbol{F}\tilde{\boldsymbol{c}}^{(j,l)}. \tag{7}$$

Thus, (7) is the discretized version of (1). If the weights are nonnegative (which implies that they are real-valued), i.e., $w_k \geq 0$ for all $k = 1, \ldots, K$, then $\boldsymbol{c}^{(j,l)}$ is real-valued as well, since all sinograms $\boldsymbol{S}^{(j)}$ and $\boldsymbol{S}^{(l)}$ are also real-valued by definition.

In the following, we choose uniform weights $w_k = 1$, $k = 1, \ldots, K$ in (6). Hence, similar to [1], we assign the same weight to all x_k from the entire available transverse domain to minimize the impact of possible noise in the sinograms. Instead of a mathematical integration (or summation as in (6)), we note that [9] and [10] use an optical integration by having the camera in the focal plane of the lens that is formed by the circular cross-section of the fiber. In that case, all the light (i.e., its integral) is focused too tightly to resolve details in the intensity profile, similar to the situation of having an x-independent coefficient $\tilde{c}_n^{(j,l)}$ after performing the sum in (6). On the other side of extremes, we could have chosen a Dirac distribution of weights that effectively evaluates (6) at only one or a few specific transverse positions x_k as in [3]. Since the algorithm that we present in the current and next section is linear, it is irrelevant if such an x-functional (integral, point evaluation, etc.) is applied before the discretization in (1) or after the discretization in (6). However, choosing a different type of functional (e.g., Dirac instead of the uniform weighting) would of course affect the accuracy and robustness of the computed optimum angle $\vartheta_{\text{best}}^{(j,l)}$ in Section IV.

With $n_{\text{best}} := \operatorname{argmax}(c_n^{(j,l)})$ being the index where the vector $\boldsymbol{c}^{(j,l)}$ from (7) has its largest entry, the associated azimuthal angle $\vartheta_{\text{best}}^{(j,l)} = \vartheta_{n_{\text{best}}}$ is the amount by which the fiber cross section at $z = z_j$ needs to be rotated to achieve optimum alignment (in the sense of being the best out of the N discrete angles $\vartheta_1, \ldots, \vartheta_N$) with the fiber cross section at $z = z_l$. Equivalently, the fiber cross section at $z = z_l$ would need to be rotated by $-\vartheta_{\text{best}}^{(j,l)}$ for optimum alignment with the cross section at $z = z_j$.

In the case of the 4-core fibers from Figs. 1–3 and [1], [4], [5], [6], the azimuthal spacing of the cores is 90°. Hence, there are $M_{\text{equiv}} = 4$ alternative ways (sectors, in this case quadrants) of aligning the cores before splicing. The continuous cross-correlation $c^{(j,l)}(\vartheta, x)$ from (1) as well as the discrete cross-correlation $\boldsymbol{c}^{(j,l)}$ from (7) as shown in Fig. 5(a) therefore has four

distinct peaks in this case of 4CF2. One of those four peaks aligns not only the cores, but also the markers (in the sense that they are then located in the same quadrant, and, if the relative polarity of the two fibers is correct "+" and both fibers have the same marker design, then the markers are in fact aligned). However, since a marker is usually small compared to the cores, it has only a minor impact on the height of these peaks in the cross-correlation. Hence, in presence of noise due to finite camera pixel size, surface imperfections on the fiber, a nonperfect equivalence of the rotation axis and the fiber center etc., there may be multiple peaks in the cross-correlation of nearly identical height as in Fig. 5(a). Therefore, the cross-correlation $\boldsymbol{c}^{(j,l)}$ from (7) is not a stable predictor of the best alignment angle.

IV. NEW SEPARATION ALGORITHM: ACCURACY AND SELECTION COMPONENT

To get a more distinct signal from the marker that allows for a reliable selection of the correct peak in the cross-correlation, we separate the cross-correlation vector $\boldsymbol{c}^{(j,l)}$ from (7) into two additive components: the "accuracy component" $\boldsymbol{c}_{\text{acc}}^{(j,l)}$ that captures those parts (usually the cores) of the transverse geometry that should be perfectly aligned azimuthally, and the "selection component" $\boldsymbol{c}_{\text{sel}}^{(j,l)}$ that comprises everything else (most importantly the marker asymmetry) to select one of several possible azimuthal alignment options of the accuracy component. Thus, (7) becomes [13], [19]

$$\boldsymbol{c}^{(j,l)} = \boldsymbol{c}_{\text{acc}}^{(j,l)} + \boldsymbol{c}_{\text{sel}}^{(j,l)} = \underbrace{\boldsymbol{F}\tilde{\boldsymbol{c}}_{\text{acc}}^{(j,l)}}_{\boldsymbol{c}_{\text{acc}}^{(j,l)}} + \underbrace{\boldsymbol{F}\tilde{\boldsymbol{c}}_{\text{sel}}^{(j,l)}}_{\boldsymbol{d}_{\text{sel}}^{(j,l)}}$$

$$= \boldsymbol{F}\underbrace{\left(\tilde{\boldsymbol{c}}_{\text{acc}}^{(j,l)} + \tilde{\boldsymbol{c}}_{\text{sel}}^{(j,l)}\right)}_{\tilde{\boldsymbol{c}}^{(j,l)}} = \boldsymbol{F}\tilde{\boldsymbol{c}}^{(j,l)}. \tag{8}$$

Each entry of the vector $\tilde{\boldsymbol{c}}_{\text{acc}}^{(j,l)}$ is either zero or identical to the same entry of the original vector $\tilde{\boldsymbol{c}}^{(j,l)}$, depending on whether this entry is part of an index set I_{acc}:

$$\left(\tilde{c}_{\text{acc}}^{(j,l)}\right)_n = \begin{cases} \tilde{c}_n^{(j,l)}, & n \in I_{\text{acc}}, \\ 0, & \text{otherwise.} \end{cases} \tag{9}$$

To guarantee that the accuracy component has exactly M_{equiv} peaks of identical height, e.g., $M_{\text{equiv}} = 4$ in the case of 4CF1 in Fig. 1(a), (b), and (c), the index set I_{acc} comprises the characteristic azimuthal frequency M_{equiv} and its harmonics, i.e.,

$$I_{\text{acc}} = \Big\{ n = 1 + \operatorname{mod}(m M_{\text{equiv}}, N), \text{ where}$$

$$m \in \mathbb{Z}, \left| m + \frac{1}{4 M_{\text{equiv}}} \right| \leq \frac{N - \frac{1}{2}}{2 M_{\text{equiv}}} \Big\}. \tag{10}$$

We note that the DC component has index $n = 1$ and that the modulo command "mod" in (10) is necessary to correctly convert the integer number m, which is from the set $\mathbb{Z}$ of integers and can therefore be negative, to the positive integer n that is used for indexing the entries in the vector $\tilde{\boldsymbol{c}}_{\text{acc}}^{(j,l)}$ in (9). The inequality at the end of (10) is necessary to avoid aliasing. The only fiber-dependent parameter of our method is the integer
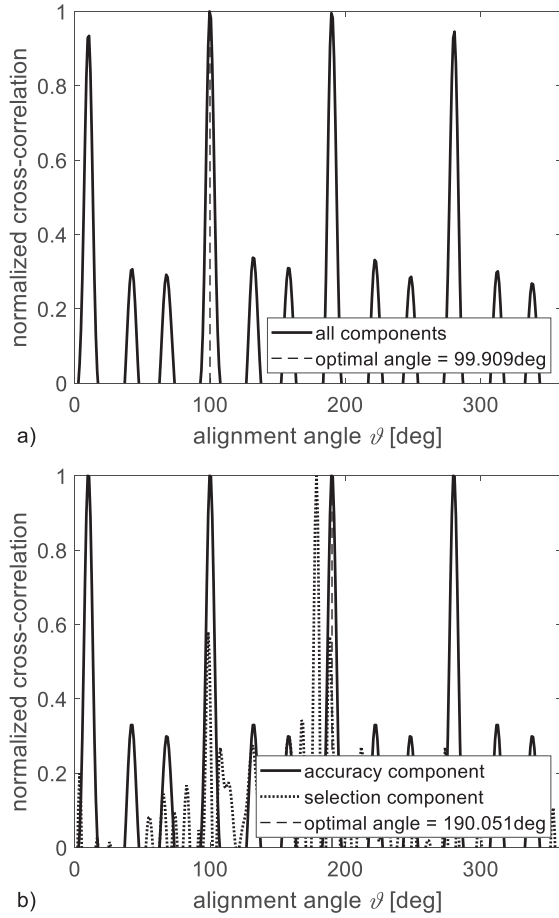
Fig. 5. (a) Global normalized cross-correlation $c^{(j,l)}$ from (7) of the two ends of 4CF2 from Fig. 4, leading to wrong quadrant (99.9°). (b) Normalized cross-correlation separated into accuracy component $c_{\text{acc}}^{(j,l)}$ and selection component $c_{\text{sel}}^{(j,l)}$ in (8), leading to correct quadrant (190°).
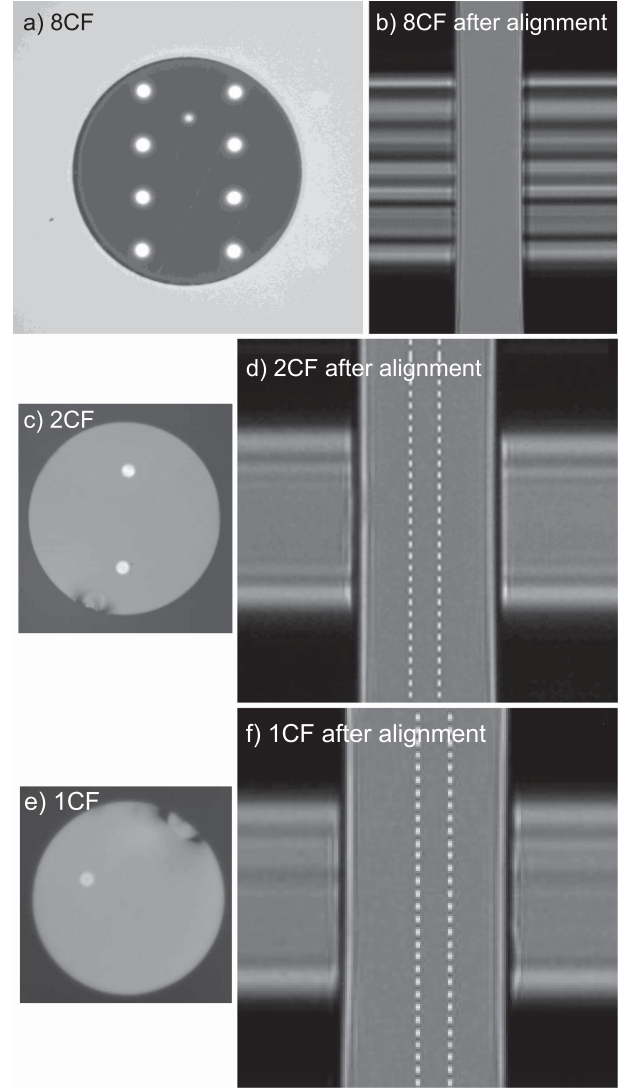

Fig. 6. End-view and side-view after alignment for other fiber examples. (a,b) 8CF. (c,d) 2CF. (e,f) 1CF, where the single core is offset from the center of the fiber.

number M_{equiv}, which is the azimuthal frequency at which the peaks in the cross-correlation $c^{(j,l)}$ from (7) reappear, see Fig. 5. The separation algorithm (8)–(10), which differentiates our work from previous methods [1], [3], [5], [9], [10], [11] that also use some sort of cross-correlation, is therefore very general and does not neglect any coefficients in the Fourier expansion, in contrast to [9], [10], [11].

Due to (8)–(10), the accuracy component $c_{\text{acc}}^{(j,l)}$ has the period $360°/M_{\text{equiv}}$, i.e., in the case of the 4-core fiber 4CF2, it has $M_{\text{equiv}} = 4$ peaks of exactly identical height (solid curve in Fig. 5(b)). The accurate azimuthal alignment angle is the location (in this case $\vartheta_{\text{best}}^{(j,l)} = 190.051°$) of that peak of the accuracy component that is closest to the single peak of the selection component $c_{\text{sel}}^{(j,l)}$ (dotted in Fig. 5(b)). This angle 190.051° is exactly the amount by which the left fiber in Fig. 4(a) needs to be rotated such that its cores align perfectly with those of the right fiber in Fig. 4(b) and such that their markers are in the same quadrant (but cannot be exactly aligned, as the relative polarity is "−"). In contrast, the highest peak of the global cross-correlation $c^{(j,l)}$ from (7) in Fig. 5(a) would have led us

to the wrong quadrant (99.909°), i.e., a 90° error corresponding to a confusion of cores, i.e., transmission channels.

Using the new alignment algorithm from (8)–(10), we reproducibly achieved perfect alignment for a wide range of fibers with completely different geometries and numbers of cores as shown in Fig. 6. The only parameter that needs to be changed in the algorithm when changing the fiber type is the number M_{equiv} in (10). The user only needs to be aware that this integer number M_{equiv} is the number of possible equivalent alignments of the cores of the two fibers, which is not necessarily identical to the total number N_{cores} of cores in either of the two fibers. For instance, while $M_{\text{equiv}} = N_{\text{cores}}$ is true for the cases in Figs. 1 and 6(c)–(f), we have $M_{\text{equiv}} = \frac{N_{\text{cores}}}{4} = 2$ in Fig. 6(a) and (b), because the eight cores of 8CF are arranged in a 2×4 array that only has a $180° = 360°/M_{\text{equiv}}$ period, instead of those eight cores being arranged on a circle with equidistant spacing of
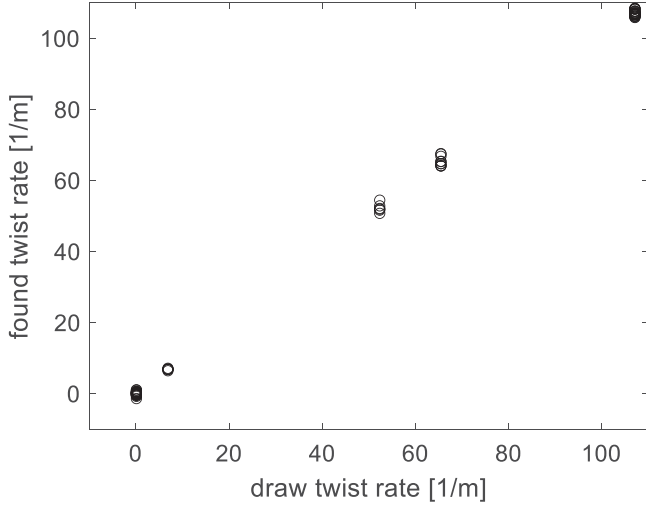
Fig. 7. Twist rates found for 4CF2 and 7CF drawn at different twist rates.

$360°/N_{cores} = 45°$. We also note that the successful alignment shown in Fig. 6(f) proves that our algorithm from (8)–(10) is not limited to MCF, but can as well be used for single-core fibers ($M_{equiv} = 1$) that have asymmetries. For single-core fibers that do not have asymmetries, both the accuracy and selection component from (8) in Fig. 5(b) would become flat (constant), in agreement with the trivial fact that such radially symmetric fibers do not require azimuthal alignment optimization.

V. DETERMINATION OF THE TWIST RATE

If side-view intensity measurements at two or more longitudinal locations are available per fiber, e.g., z_{j-2}, z_{j-1}, and z_j for the left fiber as indicated by the vertical dashed lines in Fig. 1(e), the accuracy of the alignment angle computation can be further improved by a polynomial fit. For example, if the lines $\vartheta_{fit}^{(L)}(z) = \vartheta_{fit,0}^{(L)} + a_{fit}^{(L)} z$ and $\vartheta_{fit}^{(R)}(z) = \vartheta_{fit,0}^{(R)} + a_{fit}^{(R)} z$ are the best fits to the data $(z_j, \sum_{k=1}^{j-1} \vartheta_{best}^{(k,k+1)})$ and $(z_l, \sum_{k=1}^{l-1} \vartheta_{best}^{(k,k+1)})$ in the left and right fiber, respectively, then the optimum alignment angle at the fiber end locations z_L and z_R is

$$\vartheta_{best}^{(L,R)} = \vartheta_{fit,0}^{(R)} + a_{fit}^{(R)} z_R - \vartheta_{fit,0}^{(L)} - a_{fit}^{(L)} z_L, \qquad (11)$$

and the twist rates of the left and right fiber are $\frac{a_{fit}^{(L)}}{2\pi}$ and $\frac{a_{fit}^{(R)}}{2\pi}$, respectively. Instead of a straight line, i.e., a fit of degree $d_{fit} = 1$, a higher-order fit (parabolic, cubic, etc., in general of degree $d_{fit} \geq 1$) can be used as well for the twist rate if there are at least $d_{fit}+1$ locations z_l along the particular fiber.

Found twist rates for fibers with different draw twist rates are shown in Fig. 7, with standard deviations $<1.4/m$ allowing for a reliable identification of fibers with different twist rates.

VI. DETERMINATION OF THE RELATIVE AND ABSOLUTE POLARITY

The fact that the peak of the selection component in Fig. 5(b) does not coincide with any of the peaks of the accuracy component in Fig. 5(b) indicates that the markers of these two

particular fiber ends are not aligned when the cores are aligned. The relative polarity in this case is therefore detected as wrong ("−"), whereas (after flipping the ends of one of the two fibers) it would be detected as correct ("+") when the peak of the selection component in Fig. 5(b) had coincided with a peak of the accuracy component. Thus, the *relative* polarity is automatically determined from the accuracy and selection components in (8) and Fig. 5(b) as a by-product of the above algorithm, and we found it to be correct with $>99\%$ reliability for 4CF1 and 4CF2 with 2 false relative polarity returns among more than 200 trials.

To also compute the *absolute* polarity of each fiber end, one of the two matrices in (5) needs to be removed, or, in more general terms, be replaced by a constant matrix. We therefore choose [19] a matrix $\tilde{S}^{(j)}$ in (5) with entries $\tilde{S}_{n,k}^{(j)} = a_k$ and arbitrary nonzero real-valued or complex-valued numbers $a_k \neq 0$ for $k = 1, \ldots, K$, i.e., a matrix $\tilde{S}^{(j)}$ whose rows are all identical, with weights w_k in (6) that satisfy the equation $w_k a_k^* = w_{k-1} a_{k-1}^* e^{i\gamma_{slope}}$ for $k = 2, \ldots, K$ with a real-valued number γ_{slope}. Since this is mathematically equivalent to choosing a j-independent identity matrix $\tilde{S}^{(j)} = I$, the superscript "j" of the vector $c^{(j,l)}$ in (7) can be omitted, i.e., $c_n^{(j,l)} = c_n^{(l)}$ is valid without loss of generality in the case of this single-fiber approach. In other words, the weights w_k are in this case chosen such that neighboring columns (corresponding to neighboring transverse positions t_k in (2) of the matrix $\tilde{S}^{(l)}$ in (6)) are added with relative phase shifts of γ_{slope} radians. The entries $c_n^{(l)}$ of the N-dimensional vector $c^{(j,l)} = c^{(l)}$ in (7) thus represent sums of shifted copies of the columns of the discrete sinogram $S^{(l)}$ from (2), effectively summing up the entries of $S^{(l)}$ along a direction that has the slope γ_{slope}. The reason for doing the transverse summation along a certain direction becomes obvious in the side-view sinogram example shown in Fig. 4: characteristic features that arise from the presence of cores or markers or cladding shapes etc. show up as tilted lines, and the steepness (slope) of those tilted lines increases with an increasing distance of that particular transverse feature from the fiber axis. Therefore, the optimum γ_{slope} depends on the transverse location of the feature whose signal is to be detected. For instance, since the marker is placed further away from the fiber axis than the cores in the fiber cross section in Fig. 1(a), the slope of the marker, e.g., at the azimuthal angle $\vartheta = 10°$ in the sinogram in Fig. 4(a), is steeper than the slope of the four cores that appear after every $90°$. Hence, different values of γ_{slope} may be used for cores and markers. While the slopes are being explicitly addressed by the value of γ_{slope} in this single-fiber approach (fiber-independent matrix $\tilde{S}^{(j)} = I$ in (5)), this is not necessary in the cross-correlation approach (fiber-dependent nontrivial matrix $\tilde{S}^{(j)}$ in (5)), where the slopes at the different locations z_j and z_l automatically cancel each other out due to the complex conjugate of the matrix $\tilde{S}^{(j)*}$ in (5).

Applying this single-fiber approach separately to both fiber ends [19], similar to Fig. 5, we found $>95\%$ reliability of the absolute polarity computation with 9 false returns among more than 200 trials.
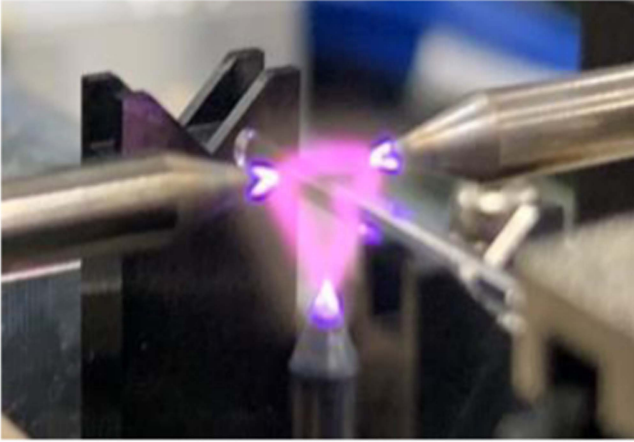
Fig. 8.   3-electrode splicing to achieve equal temperature and equally low loss for all cores.

VII. Splice Loss, Speed and Success Rate

After the alignment computation, which is performed on a laptop that is connected to the splicer, the left fiber is rotated by the computed amount ϑ_{best}, or the right fiber is rotated by $-\vartheta_{\text{best}}$, or the left fiber is rotated by $\vartheta_{\text{best}}/2$ and the right fiber by $-\vartheta_{\text{best}}/2$. Examples after alignment are shown in Figs. 1(c) and 6.

After the rotational alignment, the two fibers are fusion-spliced using the three-electrode arc-discharging S185PM ROF splicer [10] to achieve a uniform heat distribution across all cores, see Figs. 4(b) and 8. The side-view sinogram scan, alignment computation, rotation and arc time amount to only about 90 seconds with our new splicing solution. The resulting splice losses for 4CF1 and 4CF2 are shown in Fig. 9 for the fundamental LP_{01} mode at 1550 nm and 1360 nm wavelength, respectively. Splice loss is measured with a tunable laser and power meter setup through a fan-in/fan-out device. The reference power is measured through each core of an unbroken section of fiber. The fiber is then broken and repeatedly respliced with new power measurements after each resplice. Care is taken in the power measurement to ensure correct cores have been aligned. With an almost 100% alignment (correct core) success rate, we achieved average losses of 0.025 dB (4CF1, correct polarity, 10 splices), 0.022 dB (4CF2, correct polarity, 10 splices) and 0.024 dB (4CF2, wrong polarity, 10 splices). Hence, for both 4-core fiber designs, the splice loss is at the same level as for single-core fiber splicing. The fact that this is true regardless of polarity, i.e., intentional or unintentional flips of one of the two fibers to be spliced, is a substantial advantage in terms of real-world applicability in the field.

The measured splice loss is shown in Fig. 10 as a function of an intentional rotational offset for both 4CF1 and 4CF2. The measurement values at zero offset at the center of the curve in Fig. 4(c) confirm our previous result of <0.03 dB average splice loss. The fact that no nonzero offset gives similarly low splice loss confirms the optimality of the computed rotation angle.
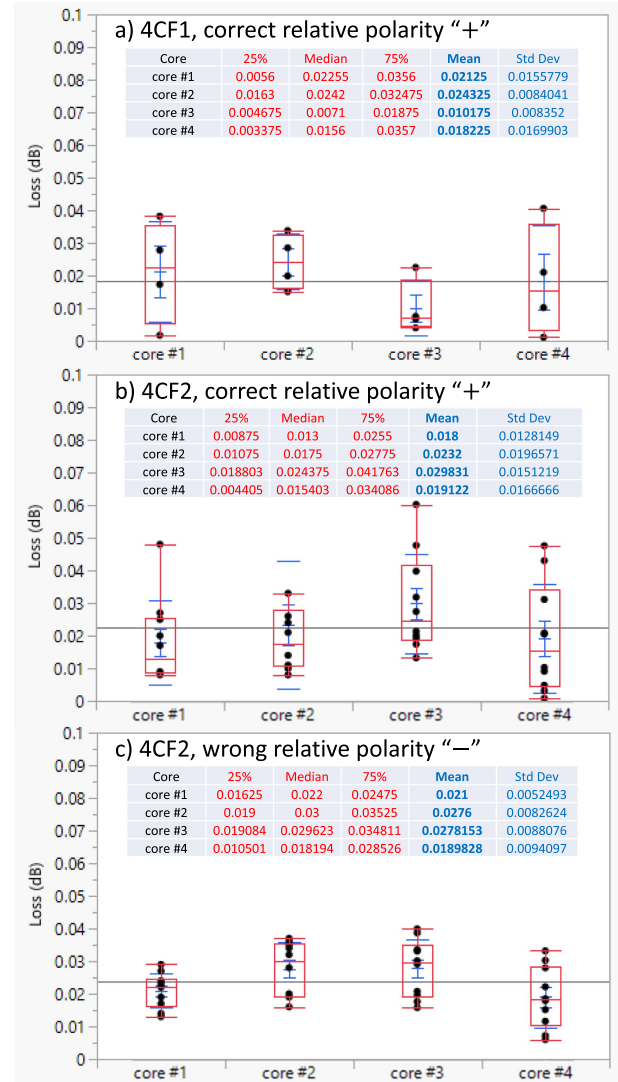

Fig. 9.   Average splice loss of 4CF1 and 4CF2 as a function of intentional rotational offset from the algorithm optimum. (a) 4CF1 with correct relative polarity "+". (b) 4CF2 with correct relative polarity "+". (c) 4CF2 with wrong relative polarity "−".

VIII. Conclusion

A novel azimuthal alignment algorithm is presented for optical fibers that are not circularly symmetric, e.g., multicore fibers with or without markers or D-shaped cladding as well as single-core fibers with stress rods (polarization maintaining fibers) or offset single-core fibers. The cross-correlation of the side-view sinograms of the two fibers to be spliced is separated into an accuracy component, which contains the azimuthal periodicity of the core layout, and a selection component that locates all intentional and unintentional asymmetries of the fiber. The selection component is used to select the correct peak, i.e., the correct core combination, of the accuracy component, which is then used to accurately quantify the optimum alignment angle. This algorithm also determines the relative polarity of the two fibers as a by-product, and a modified version of the algorithm that uses
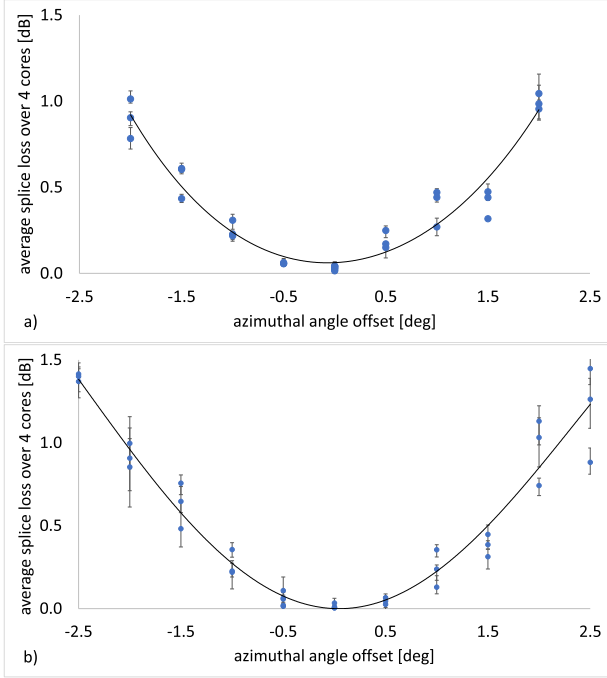
Fig. 10.   Average splice loss of 4CF as a function of intentional rotational offset from the algorithm optimum. (a) 4CF1 at 1360 nm [18]. (b) 4CF2 at 1550 nm.

only a single side-view sinogram can be used to identify the absolute polarities of both fibers with very high reliability as well. The twist rates of the two fibers in the splicer are computed by line fits to repeated measurements and computations at different longitudinal locations, with standard deviations of less than 1.4/m for a 7-core fiber. Using this algorithm, we achieve an almost 100% alignment success rate for a wide range of fibers with completely different geometries and numbers of cores. In combination with a 3-electrode arc-discharging Fitel S185PM ROF splicer, we consistently achieved splicing times of only 90 seconds and single-core-fiber-like splice losses of less than 0.03 dB on average for two different 4-core fiber designs. This very low loss is achieved regardless of polarity, i.e., intentional or unintentional flips of one of the two fibers to be spliced, which is a substantial advantage in terms of real-world applicability in the field.

APPENDIX
EQUIDISTANT ANGLES FOR FFT

While in general the spacing between adjacent measurement points ϑ_n, x_k and z_l in (2) may vary, in the special case of equidistant azimuthal angles with spacing $\Delta\vartheta$,

$$\vartheta_n = \vartheta_1 + (n-1)\underbrace{\frac{2\pi}{N}}_{=\Delta\vartheta}, \qquad n = 1, \ldots, N, \qquad (12)$$

the elements of the matrix $\boldsymbol{F}$ defined in (3) become

$$F_{n,m} = \frac{1}{N}e^{i(m-1)\left(\vartheta_1 + \frac{2\pi(n-1)}{N}\right)}$$

$$= \underbrace{\frac{1}{N}e^{i2\pi\frac{(n-1)(m-1)}{N}}}_{=\text{IFFT}_{n,m}} \underbrace{e^{i(m-1)\vartheta_1}}_{=\Theta_{m,m}}, \; n, m = 1, \ldots, N. \tag{13}$$

In this case, the matrix $\boldsymbol{F}$ from (3) is the product of a uniform discrete inverse Fourier transform (IDFT) matrix that can be efficiently applied with the Inverse Fast Fourier Transform (IFFT) algorithm, and a unitary diagonal matrix $\boldsymbol{\Theta} = \left(\boldsymbol{\Theta}^\dagger\right)^{-1} = \left(\boldsymbol{\Theta}^*\right)^{-1}$, where the dagger symbol "$\dagger$" indicates complex conjugate transpose. As an example, (7) becomes

$$\boldsymbol{c}^{(j,l)} = \text{IFFT}\left(\boldsymbol{\Theta}\tilde{\boldsymbol{c}}^{(j,l)}\right). \tag{14}$$

Similarly, the inverse matrix $\boldsymbol{F}^{-1}$ can be efficiently computed with a Fast Fourier Transform (FFT). When applied to a matrix, the FFT and IFFT discussed here are one-dimensional transformations that separately transform the individual columns, in agreement with the IDFT matrix element definition in (13). As an example, (4) becomes

$$\tilde{\boldsymbol{S}}^{(l)} = \boldsymbol{F}^{-1} \boldsymbol{S}^{(l)} = \boldsymbol{\Theta}^{-1} \text{FFT}\left(\boldsymbol{S}^{(l)}\right). \tag{15}$$

This option of using the highly efficient FFT and IFFT algorithms applies for all appearances of the matrix $\boldsymbol{F}$ and its inverse $\boldsymbol{F}^{-1}$, provided that the equidistance condition (18) is valid.

It is noted that the choice of the first angle ϑ_1 in (12), and thus the matrix $\boldsymbol{\Theta}$ in (14) and (15), is completely irrelevant for the following mathematical reasons: The matrix $\tilde{\boldsymbol{C}}^{(j,l)}$ in (5) is independent of $\boldsymbol{\Theta}$ due to $\boldsymbol{\Theta}^{-1*} = \boldsymbol{\Theta}$ and $\tilde{\boldsymbol{C}}^{(j,l)} = \tilde{\boldsymbol{S}}^{(j)*} \odot \tilde{\boldsymbol{S}}^{(l)} = \left(\boldsymbol{\Theta} \, \text{FFT}(\boldsymbol{S}^{(j)})^*\right) \odot \left(\boldsymbol{\Theta}^{-1}\text{FFT}(\boldsymbol{S}^{(l)})\right) = \text{FFT}(\boldsymbol{S}^{(j)})^* \odot \left(\boldsymbol{\Theta}\boldsymbol{\Theta}^{-1}\text{FFT}(\boldsymbol{S}^{(l)})\right) = \text{FFT}(\boldsymbol{S}^{(j)})^* \odot \text{FFT}(\boldsymbol{S}^{(l)})$, where the fact that diagonal matrices can be moved from one side of the element-wise product "$\odot$" to its other side without changing the result is used. Due to (6), the vector $\tilde{\boldsymbol{c}}^{(j,l)}$ in (14) is then also independent of $\boldsymbol{\Theta}$. Finally, since a Fourier transform relates a linear phase with a constant shift, the matrix $\boldsymbol{\Theta}$ in (14) shifts the cross-correlation $\boldsymbol{c}^{(j,l)}$ by the amount ϑ_1. Hence, a plot of the discrete values $c_n^{(j,l)}$ vs. the discrete angles ϑ_n always looks exactly the same regardless what value is chosen for the first angle ϑ_1. Without loss of generality, it may be assumed that $\vartheta_1 = 0$, which leads to a unit matrix $\boldsymbol{\Theta} = \boldsymbol{I}$ that is trivial and can be omitted in all computations.

The computation of (14) and (15) can be further simplified and accelerated by taking advantage of the fact that $\boldsymbol{S}^{(j)}$, $\boldsymbol{S}^{(l)}$ and $\boldsymbol{c}^{(j,l)}$ are real-valued. Therefore, the entries $\tilde{S}_{n,k}^{(l)}$ of the matrix $\tilde{\boldsymbol{S}}^{(l)}$ in (15) satisfy the symmetry property (without loss of generality assuming $\boldsymbol{\Theta} = \boldsymbol{I}$) $\tilde{S}_{n,k}^{(l)} = \tilde{S}_{1+\text{mod}(1-n,N),k}^{(l)*}$ for $n = 1, \ldots, N$ and $k = 1, \ldots, K$.

REFERENCES

[1] K. Saito, T. Sakamoto, T. Matsui, K. Nakajima, and T. Kurashima, "Side-view based angle alignment technique for multi-core fiber," in *Proc. Opt. Fiber Commun. Conf.*, 2016, doi: 10.1364/OFC.2016.M3F.3.

[2] W. Zheng, "Automated alignment and splicing for multicore fibers," in *Proc. Opt. Fiber Commun. Conf.*, 2013, doi: 10.1364/OFC.2013.OM3I.4.

[3] W. Zheng, D. Duke, T. Kubo, and B. Malinsky, "Interrelation profile analysis method for alignment of polarization-maintaining fiber," in *Proc. Opt. Fiber Commun. Conf.*, 2010, doi: 10.1364/NFOEC.2010.JthA61.

[4] M. Ohzeki, "Alignment and fusion splicing techniques for MCFs," in *Proc. Eur. Conf. Opt. Commun. Workshop Mo1A-WS*, 2021.

[5] M. Ohzeki, Y. Sasaki, K. Takenaga, K. Ichii, and K. Aikawa, "Side-view rotational alignment method for trench-assisted 4-core fibers," in *Proc. Opt. Fiber Commun. Conf.*, 2022, doi: 10.1364/OFC.2022.M4E.4.

[6] M. Takahashi, T. Fujii, R. Sugizaki, M. Tsukamoto, and Y. Arashitani, "Field usable fusion splicing technique for multicore fiber," in *Proc. IEEE Photon. Soc. Summer Topicals Meeting Ser.*, 2020, doi: 10.1109/SUM48678.2020.9161043.

[7] W. Ji, R. Yu, Z. Shen, C. Wang, C. Xiong, and L. Xiao, "Low-loss fusion splicing between spacing-mismatched multicore fibers," *Opt. Lett.*, vol. 46, no. 24, pp. 6112–6115, 2021, doi: 10.1364/OL.447602.

[8] M. Suzuki, H. Yoshii, T. Ito, Y. Yamamoto, T. Hayashi, and T. Hasegawa, "Low loss splicing between coupled multi-core fibers with thermally expanded cores," in *Proc. Opt. Fiber Commun. Conf.*, 2018, Paper Tu3B.5, doi: 10.1364/OFC.2018.Tu3B.5.

[9] W. Zheng, "Auto-aligning and splicing PM-fibers of different types with a passive method," *Proc. SPIE*, vol. 2837, pp. 356–367, 1996, doi: 10.1117/12.258197.

[10] W. Zheng, "Automated fusion-splicing of polarization maintaining fibers," *J. Lightw. Technol.*, vol. 15, no. 1, pp. 125–134, Jan. 1997, doi: 10.1109/50.552120.

[11] W. Zheng, H. Sugawara, and B. Malinsky, "Fourier analysis method for asymmetric polarization-maintaining fiber," in *Proc. Opt. Fiber Commun. Conf.*, 2012, paper JW2A.12, doi: 10.1364/NFOEC.2012.JW2A.12.

[12] Y. Amma, A. Takahashi, K. Takenaga, and S. Matsuo, "Accuracy of core alignment with end-view function for multicore fiber," in *Proc. IEEE Photon. Soc. Summer Topicals Meeting Ser.*, 2014, pp. 170–171, doi: 10.1109/SUM.2014.94.

[13] T. Kremp, Y. Liang, and A. H. McCurdy, "Less than 0.03 dB multicore fiber passive fusion splicing using new azimuthal alignment algorithm and 3-electrode arc-discharging system," in *Proc. Eur. Conf. Opt. Commun.*, 2022, paper Tu3A.3.

[14] [Online]. Available: https://www.furukawa.co.jp/splicer/en/product/s185 pmrof.html

[15] M. Takahashi et al., "Uncoupled 4-core fibre with ultra-low loss and low inter core crosstalk," in *Proc. Eur. Conf. Opt. Commun.*, 2020, doi: 10.1109/ECOC48923.2020.9333161.

[16] T. Allsop et al., "Bending and orientational characteristics of long period gratings written in D-shaped optical fiber [directional bend sensors]," *IEEE Trans. Instrum. Meas.*, vol. 53, no. 1, pp. 130–135, Feb. 2004, doi: 10.1109/TIM.2003.821508.

[17] P. S. Westbrook et al., "Continuous multicore optical fiber grating arrays for distributed sensing applications," *J. Lightw. Technol.*, vol. 35, no. 6, pp. 1248–1252, Mar. 2017, doi: 10.1109/JLT.2017.2661680.

[18] T. Kremp, Y. Liang, and A. H. McCurdy, "Polarity and twist rate detection for accurate and reliable low loss multicore fiber fusion splicing," in *Proc. Opt. Fiber Commun. Conf.*, 2023, Paper Tu2C.1.

[19] T. Kremp, Y. Liang, and R. L. Lingle, International Patent Application WO2022/125443A1, Jun. 16, 2022.

Tristan Kremp (Senior Member, Optica) received the Dipl.-Ing. (M.S.) and the Dr.-Ing. (Ph.D.) degrees in electrical engineering from the Karlsruhe Institute of Technology, Karlsruhe, Germany, in 1998 and 2002, respectively, and the Dr.rer.nat. (Ph.D.) degree in mathematics from Institut für Geometrie und Praktische Mathematik, RWTH Aachen University, Aachen, Germany. From 2002 to 2008, he was with the Institut für Geometrie und Praktische Mathematik, RWTH Aachen University. In 2008, he joined OFS Laboratories, where he is a Distinguished Member of Technical Staff. He was the recipient of multiple awards for his work, which covers a wide range of optical and microwave applications of electromagnetic field simulations, including the design and analysis of hollow core fibers and Bragg gratings, multimode fiber imaging with classical and machine learning methods, mode coupling in waveguides and laser cavities, the development of highly efficient wavelet, spectral and quasi-spectral methods for nonlinear optical pulse propagation and multicore fiber splicing, and time domain solutions for scattering problems.

Yue Liang (Member, IEEE) received the Ph.D. degree from Chemical Engineering Department, Kyoto University, majoring in process system engineering. He is currently a Technical Manager for Network System and Fusion Splicer, OFS. He is extensively involved in various fiber splicing technologies' development, optimizations, and implementations. His research interests include how to align and splice multiple core fibers, hollow core fibers, and various ribbon fibers. Before joining OFS, he was with Mobil Technologies Research in Dallas and Furukawa Electric in Japan and U.S.

Alan H. McCurdy (Member, IEEE) received the B.S. degrees in chemical engineering and physics from Carnegie Mellon University, Pittsburgh, PA, USA, and the Ph.D. degree from Yale University, New Haven, CT, USA. After teaching electrical engineering with the University of Southern California, Los Angeles, CA, USA, through most of the 1990s, he moved to Lucent Technologies, where he focused on solving noise problems in copper LAN networks. He transitioned to optics in the early 2000s and joined OFS in 2001. He is currently a Distinguished Member of Technical Staff doing technical business case development and support for new fiber products, marketing of the same, and, when time allows, works on advanced noise and fiber measurement problems in optical communications.